Inorganic Chemistry

pubs.acs.org/IC

Article

Flux Growth, Crystal Structure, and Chemical Bonding of Yb_2PdGe_3, an AlB_2 Superstructure within the Rare-Earth Series

Riccardo Freccero,* Laura C. J. Pereira, Pavlo Solokha, and Serena De Negri

Cite This: *Inorg. Chem.* 2023, 62, 1988−1999

Read Online

ACCESS | Metrics & More | Article Recommendations | Supporting Information

ABSTRACT: The complete structure revision of the RE_2PdGe_3 (*RE* = rare-earth metal) series revealed that Yb_2PdGe_3 is the only AlB_2 ordered superstructure. Good-quality single crystals of this compound were successfully grown from molten indium flux, enabling accurate single-crystal investigations. Yb_2PdGe_3 crystallizes with the Ce_2CoSi_3-type structure in the hexagonal space group *P6/mmm* (no. 191) with lattice parameters $a = 8.468(1)$ Å and $c = 4.0747(7)$ Å. This structure is a four-order derivative of AlB_2, composed of planar $^2_\infty[PdGe_3]$ honeycomb layers spaced by Yb species, located at the center of Ge_6 and Ge_4Pd_2 hexagons. A superconducting transition is observed below the critical temperature of 4 K. A divalent state of Yb is deduced from magnetic susceptibility measurements below room temperature, which indicate an almost nonmagnetic behavior. A charge transfer from Yb to Pd and Ge was evidenced by the Quantum Theory of Atoms in Molecules (QTAIM) effective charges; polar four-atomic Ge−Pd/Yb and two-atomic Pd−Yb bonds were observed from the ELI-D (electron localizability indicator), partial ELI-D, and ELI-D/QTAIM intersections. The bonding interactions between Ge atoms within regular Ge_6 hexagons are found to be intermediate between single bonds, as in elemental Ge, and higher-order bonds in the hypothetic Ge_6H_6 and Ge_6^{6-} aromatic molecules.

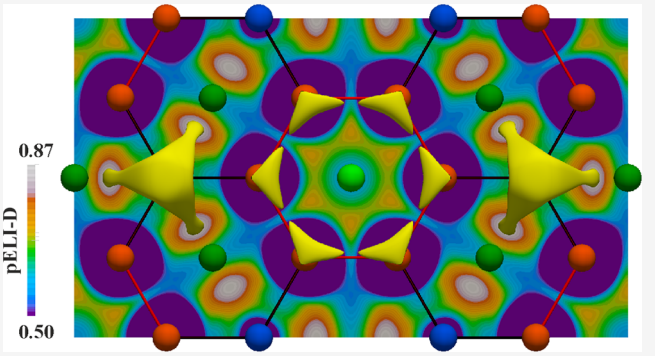

1. INTRODUCTION

Ternary rare-earth tetrelides *RE*−*T*−*Tt* (*RE* = rare-earth metal; *T* = transition metal; *Tt* = tetrel element) have been heavily studied due to their intriguing structure peculiarities, unconventional physical properties, and unprecedented bonding scenarios.[1−10] Among them, intermetallics crystallizing with a disordered AlB_2-type structure or with one of its ordered derivatives[11] have attracted particular attention since the discovery of superconductivity with $T_c \sim 39$ K in MgB_2,[12] featuring similar honeycomb-like layers. Unfortunately, investigations of physical properties of these compounds were frequently not accompanied by accurate and in-depth structural analyses, which are indeed crucial to enable a correct interpretation of the observed phenomena. This is the case for compounds with 33.3 atom % *RE*; 16.7 atom % Pd; and 50.0 atom % *Tt* nominal composition, corresponding to the 2:1:3 stoichiometry.[13] As shown in Table 1, both silicides and germanides were found to exist with almost all of the *RE*s.[14]

Most of the silicides were first reported as *hP*24-Lu_2CoGa_3, an ordered superstructure of AlB_2,[11] and subsequently revised in some cases as disordered, i.e., *hP*3-AlB_2, based on more accurate structural investigations. The Eu-containing compound is the only one crystallizing with the *hP*12-Ce_2CoSi_3 structure, which is an AlB_2 derivative as well.[11] Moving to Ge, no superstructures have been reported;[15] nevertheless, a complete structure determination was performed only in a few cases, i.e., with Ce, Nd, and Ho. Although many of such phases have been described as disordered and assigned to the AlB_2 type, they were often referred to with the misleading RE_2PdTt_3 formula, instead of $RE(Pd_xGe_{1-x})_2$ (with $x = 0.25$). Additionally, it is worth mentioning that the formation of an ordered Lu_2CoGa_3 or Ce_2CoSi_3 superstructure would lead to symmetrically inequivalent *RE* sites, which must be considered to correctly interpret the measured magnetic properties. In fact, both ferro[16−18] and antiferromagnetic[13,17] order were detected in several cases. Interestingly, "Y_2PdGe_3" is the only representative displaying a superconducting behavior below ~3 K.[16,19] Given this unique feature and the less accurate crystallographic data reported for the germanides with respect to the silicides, a complete structural reinvestigation along the whole *RE* series was performed for the "RE_2PdGe_3" phases, paying particular attention to the possible formation of ordered structures. As the main focus of this paper, we report on the

Received: September 16, 2022
Published: January 20, 2023

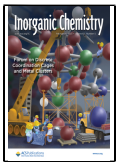

https://doi.org/10.1021/acs.inorgchem.2c03303
Inorg. Chem. 2023, 62, 1988−1999

Table 1. Crystal Structures Reported in the Literature for *RE*–Pd–{Si, Ge} Phases of 2:1:3 Composition[a]

	RE															
	Sc	Y	La	Ce	Pr	Nd	Sm	Eu	Gd	Tb	Dy	Ho	Er	Tm	Yb	Lu
Si	–	●	–	● ◆	● ●	● ◆	●	◆	● ◆	● ◆	● ◆	● ◆	● ◆	● ◆	●	◆
Ge	–	●	●	◆	●	◆	●	●	●	●	●	◆	–	–	●	–

● *hP*24–Lu_2CoGa_3 SG: $P6_3/mmc$ № 194

◆ *hP*12–Ce_2CoSi_3 SG: $P6/mmm$ № 191

●/◆ *hP3*–AlB_2 SG: $P6/mmm$ № 191

[a]● indicates that only cell parameters and the structure type were assigned and ◆ indicates a complete structure determination.

successful synthesis of the novel Yb_2PdGe_3 intermetallic, prepared both from metal flux (indium) and by direct synthesis. Its crystal structure solution and group–subgroup relations with AlB_2 are presented together with magnetic properties and chemical bonding analysis. In fact, the involved elements together with the structural features based on Ge–Ge interactions suggest approaching the chemical bonding, applying the Zintl–Klemm concept. To explain the deviations from this ideal model, it is necessary to investigate the alternative ways through which the system compensates for insufficient charge transfer and electron deficiency. For instance, in molecular chemistry, this is achieved by the formation of multiple bonds comprising π-interactions as in aromatic molecules. The similarity between the honeycomb-like layers in the compounds of interest and the widespread hexagonal aromatic cycles, together with previous studies on intermetallic π-systems,[20−22] inspired a comparative chemical bonding analysis between Yb_2PdGe_3 and ad hoc simulated molecular analogues. This contribution highlights the importance of a more general perspective in studying chemical bonding, overcoming the classic boundaries between solid-state and molecular chemistry.

2. EXPERIMENTAL SECTION

2.1. Synthetic Procedures. Samples of nominal composition 33.3 atom % *RE*; 16.7 atom % Pd; and 50.0 atom % Ge (*RE* = Y, La–Nd, Sm, Gd–Er, Yb) were synthesized to check for the existence of the ordered RE_2PdGe_3 phase. The starting materials were rods of the rare-earth metals (supplied by NewMet Ltd., Waltham Abbey, U.K.) with a freshly cleaned surface, palladium foils, and germanium chunks (supplied by MaTecK, Jülich, Germany), all with a nominal purity > 99.9 mass %. Ingots of about 0.8 g were obtained by melting stoichiometric amounts of the pristine elements.

Samples with *RE* = Y, La–Nd, Gd, Tb, Er were prepared by arc melting on a water-cooled copper heart with a tungsten electrode under ∼1 bar of Ar gas. The obtained alloys were flipped and arc-melted multiple times, ensuring their homogeneity. Weight losses were always lower than 1%.

Samples with *RE* = Sm, Dy, Ho, Yb were prepared by induction melting of the elements enclosed in arc-welded Ta crucibles to avoid element losses. The melting procedure was performed under a continuous argon flow, to prevent the high-temperature oxidation of the crucible, and repeated several times to guarantee homogeneity. These samples were characterized both in the as-cast state and after annealing at 800 °C for 3 weeks.

To obtain single-phase samples of Yb_2PdGe_3 necessary for physical properties measurements, stoichiometric amounts of the constituents were inserted in an arc-welded Ta crucible and then closed in an evacuated quartz ampoule to avoid oxidation. Subsequently, the ampoule was hung in a resistance furnace and submitted to the following thermal cycle while rotating at a speed of 100 rpm: heating (10 °C min^{-1}) up to 750 °C; heating (1 °C min^{-1}) up to 950 °C; cooling (∼0.2 °C min^{-1}) down to 800 °C. Then, the rotation was disabled, the sample kept at 800 °C for 1 week, and finally water quenched. The resulting alloy of metallic luster was ground to fine powders in an agate mortar and pressed into a pellet. The pellet was enclosed in an arc-sealed Ta crucible, put in an evacuated quartz phial, and annealed at 800 °C for 1 month prior to quenching in water.

Single crystals of Yb_2PdGe_3 suitable for X-ray diffraction analysis were grown from an indium flux. For this purpose, stoichiometric amounts of Yb, Pd, and Ge giving the $Yb_{33.3}Pd_{16.7}Ge_{50.0}$ nominal composition were placed in an arc-sealed Ta crucible with 1:45 molar excess of In (chunk, 99.99%, supplied by NewMet Ltd., Waltham Abbey, U.K.). The total mass was of about 3 g. Thus, the Ta crucible, closed in an evacuated quartz ampoule, was hung in a resistance furnace, heated up to 750 °C in about 1 h, and kept at that temperature for 1 day. Then, it was cooled to room temperature in 24 h. During the whole treatment, a continuous rotation at 100 rpm was applied.

Aiming at separating the single crystals of Yb_2PdGe_3 from the In flux, pieces of the obtained ingot were laid down on a glass wool filter and sealed in a quartz tube. The specimen was then preheated at 300 °C in a resistance furnace and centrifugated at a speed of 600 rpm for about 1 min. This procedure was repeated several times, enabling to obtain shiny gray crystals of Yb_2PdGe_3. Residual indium deposited on the crystal surfaces was selectively oxidized by immersion and sonication of the crystals in glacial acetic acid for about 2 h.

2.2. Scanning Electron Microscopy and Elemental Analysis. Metallographic analysis was performed on each sample. Small pieces were embedded in a conductive carbon-containing phenolic resin by means of an automatic hot compression mounting press Opal 410 (ATM GmbH, Germany) and submitted to a multistep grinding (SiC papers from 600 to 1200 mesh) and polishing (from 6 to 1 μm diamond pastes) procedure with the aid of an automatic polishing machine Saphir 520 (ATM GmbH, Germany). After each polishing step, sample surfaces were cleaned for a few minutes in an ultrasonic bath using petroleum ether. Several Yb_2PdGe_3 single crystals separated from the In flux were placed on a conductive carbon resin and analyzed as such. Microstructure examination as well as semiquantitative elemental analysis of the observed phases were performed using a scanning electron microscope (SEM) Zeiss Evo 40 (Carl Zeiss SMT Ltd., Cambridge, England), equipped with an energy dispersive X-ray (EDX) spectroscope from Oxford Instruments (INCA X-ACT). The calibration was effectuated on a cobalt standard.

2.3. X-ray Diffraction (XRD) Experiments. Single crystals of Yb_2PdGe_3 with metallic luster were extracted both from the mechanically fragmented sample prepared by direct synthesis and from the metal flux medium (In) after suitable centrifugation and selective oxidation. Due to their quality (see Figure 1), the flux-separated crystals were measured by single-crystal X-ray diffraction. A complete data set was obtained in a routine fashion at ambient

https://doi.org/10.1021/acs.inorgchem.2c03303
Inorg. Chem. 2023, 62, 1988−1999

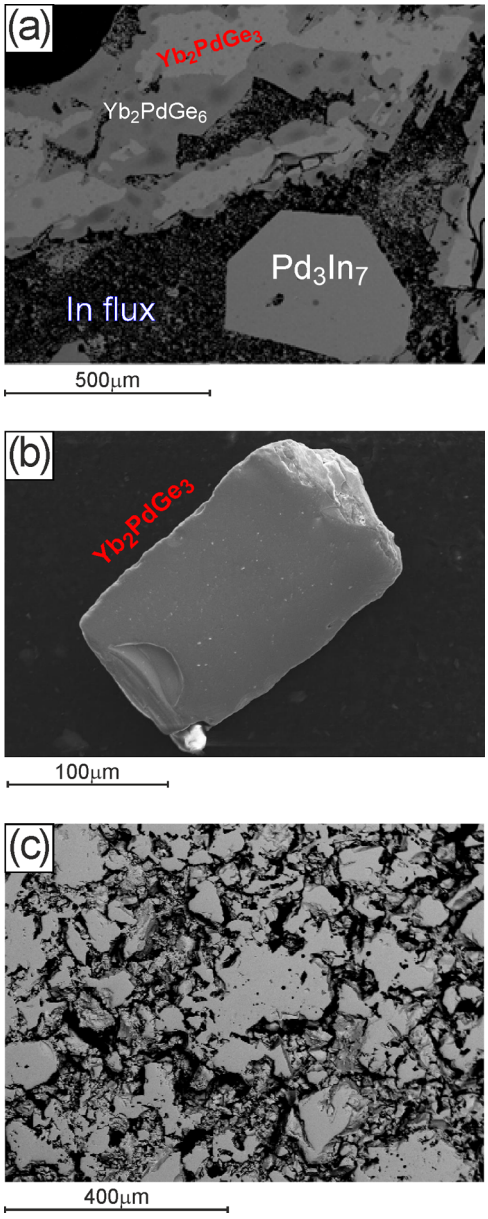

Figure 1. SEM micrographs of Yb−Pd−Ge samples: (a) synthesized by flux method, prior In removal (bulk)-BSE mode; (b) synthesized by flux method, after In removal (single crystal)-SE mode; and (c) obtained by direct synthesis followed by sintering at 800 °C-BSE mode.

conditions on a three-circle Bruker Kappa APEXII CCD area-detector diffractometer equipped by the graphite monochromatized Mo Kα (λ = 0.71073 Å) radiation, operating in ω-scan mode. Crystals were glued on glass fibers, mounted on a goniometric head, and placed in the goniostat. Intensity data were collected over the reciprocal space up to ~30° in θ (achieving a ~0.7 Å resolution) with exposures of 20 s per frame.

Data collection was performed, and the unit cell was initially refined using APEX4 [v2021.10-0].[23] Successively, data were reduced using SAINT [v8.30A][24] and XPREP [v2014/2].[25] Lorentz, polarization, and absorption effects were corrected using SADABS [v2016/2].[26] The structure was solved and refined with the aid of the programs JANA2006[27] and SHELXL-2019/1.[28]

The corresponding CIF file, available in the Supporting Information, has been deposited at the Cambridge Database with the depository number CSD-2230957. Selected crystallographic data and structure refinement parameters for the studied single crystal are listed in Table 2. Details on the structure solution are discussed in Section 3.2.

Table 2. Crystallographic Data for Yb_2PdGe_3

empirical formula	Yb_2PdGe_3
EDXS data	$Yb_{34.2}Pd_{17.6}Ge_{48.2}$
space group, Z	$P6/mmm$, 2
Pearson's symbol/prototype	$hP12$-Ce_2CoSi_3
M_w[g/mol]	670.42
a [Å]	8.468(1)
c [Å]	4.0747(7)
V [Å^3]	253.06(7)
calc. density [g/cm^3]	8.796
abs coeff (μ), mm^{-1}	57.5
unique reflections	204
reflections $I > 2\sigma(I)$	200
R_{sigma}	0.0143
data/parameters	204/13
GOF on F^2 (S)	1.46
R indices [$I > 2\sigma(I)$]	R_1 = 0.0188; wR_2 = 0.0782
R indices [all data]	R_1 = 0.0193; wR_2 = 0.0785
$\Delta\rho_{fin}$(max/min), [e/Å^3]	1.74/−1.67

X-ray powder diffraction (XRPD) measurements were performed on all samples using a Philips X'Pert MPD vertical diffractometer (Cu Kα radiation, λ = 1.5406 Å, graphite crystal monochromator, PIXcel^{1D} detector). Rietveld refinement was conducted using the Fullprof[29] software on the powder pattern of the sample submitted to physical properties measurements.

2.4. Physical Properties Measurements. Magnetic measurements were carried out using a 7 T Squid magnetometer (S700 X from Cryogenics, Ltd.) on a polycrystalline sample with an approximate mass of 10−20 mg inside a transparent capsule of 5 mm diameter. Diamagnetic signals from the gelatine capsule and straw were corrected; ZFC (zero-field cooling) and FC (field cooling) magnetic susceptibility curves were taken at different DC magnetic fields, (2.5, 5, and 10 mT) in the temperature range 1.6−300 K. Isothermal magnetization curves and hysteresis loops up to 5 T at selected temperatures were also obtained.

2.5. Computational Details. The electronic structure of Yb_2PdGe_3 was calculated by means of the all-electron full-potential local-orbital FPLO code[30,31] using the experimentally determined structure. The local spin density approximation (LSDA) to the density functional theory (DFT) as parametrized by Perdew and Wang (PW)[32] were employed to account for exchange and correlation. Relativistic effects were treated at the scalar-relativistic level. Moreover, the LSDA+U method was applied due to the localized nature of the Yb 4f states. The on-site Coulomb repulsion parameter U was set to the characteristic FPLO value of 8 eV.[33,34] The atomic limit (AL) method was selected as the double-count correction scheme. The Brillouin zone was sampled with a (4 4 8) k-point mesh. Position-space chemical bonding analysis was performed by combining topological analysis of the electron density (ED) and the electron localizability indicator, in its ELI-D[35−37] representation, using the software DGrid.[38,39] The two scalar fields were both calculated in an equidistant grid of about 0.05 Bohr using an implemented module within the FPLO code.[40] The ED was analyzed within the framework of the Bader's Quantum Theory of Atoms In Molecules (QTAIM).[41] For this purpose, the crystal space was partitioned into nonoverlapping and space-filling regions, the atomic basins, based on the gradient vector field of the ED. Its integration within each QTAIM atom gives its average electronic population that is subtracted from the atomic number providing the atomic effective charges (Q^{eff}). The application of the same procedure to the ELI-D separates the crystal space into core and valence basins, giving access to bonding interactions among the constituents. Molecular calculations for hexagermanbenzene, Ge_6H_6, and Ge_6^{6-} were effectuated

https://doi.org/10.1021/acs.inorgchem.2c03303
Inorg. Chem. 2023, 62, 1988−1999

Table 3. Results of SEM/EDXS/XRPD Characterization for $Yb_{33.3}Pd_{16.7}Ge_{50.0}$ Samples Prepared by Metal Flux (#1) and Direct Synthesis in Resistance Furnace (#2)

		composition by (EDXS) [atom %]					lattice parameters [Å]		
sample code synthesis	phases	Yb	Pd	Ge	In	Pearson symbol prototype	*a*	*b*	*c*
#1	Yb_2PdGe_3	34.2(3)	17.6(4)	48.2(3)		*hP*12-Ce_2CoSi_3	8.474(2)		4.073(2)
	Yb_2PdGe_6	23.0(2)	12.1(2)	64.9(1)		*oS*72-$Ce_2(Ga_{0.1}Ge_{0.7})_9$	8.150(2)	7.990(1)	21.847(5)
	Pd_3In_7		31.4(3)		68.6(3)	*cI*40-Ru_3Sn_7	9.4275(6)		
	Ge			100.0		*cF*8-C	5.654		
#2	Yb_2PdGe_3	34.6(6)	16.9(7)	48.5(7)		*hP*12-Ce_2CoSi_3	8.4629(4)		4.0733(4)

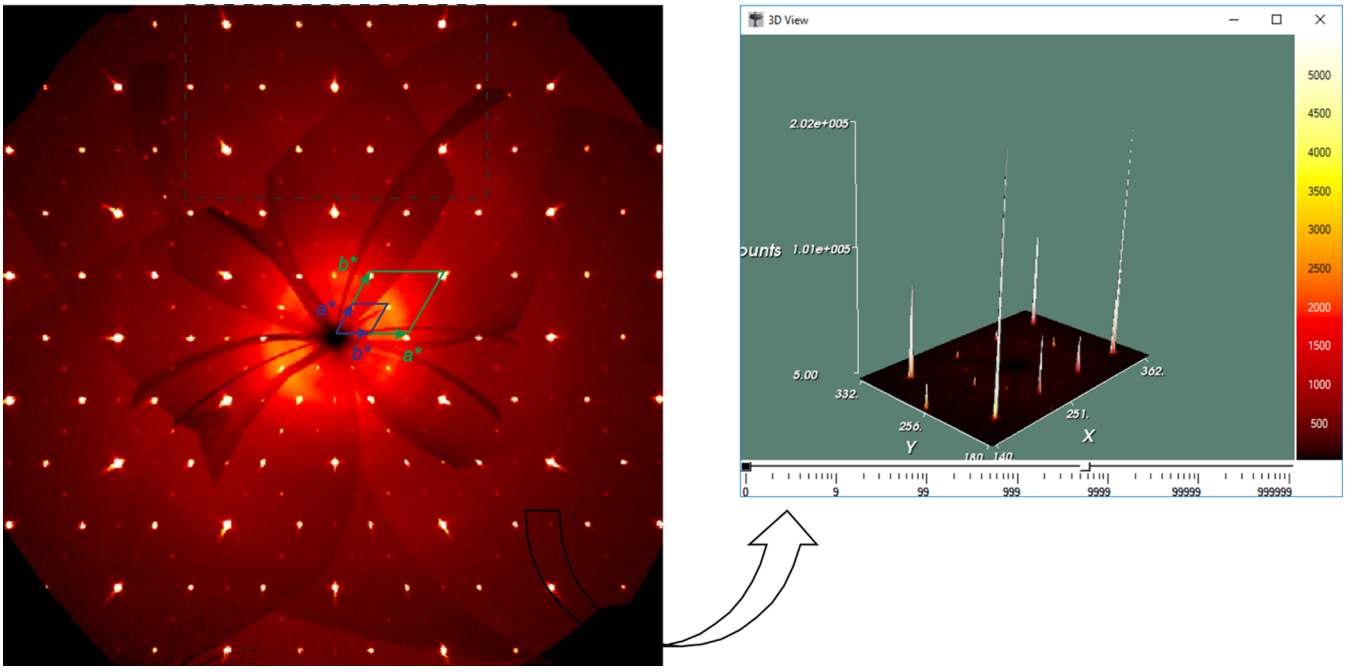

Figure 2. Intensity profiles for *hk*0 zone, with the unit cells of AlB_2 parent type (green) and of the Yb_2PdGe_3 superstructure (blue). The presence of weak superreflections is well visible in the 3D view (on the right).

with the all-electron FHI-aims software. Atomic coordinates were optimized starting from planar geometries using the LDA/PW, GGA/PBE,[42] and B3LYP[43] exchange and correlation functionals. For both Ge and H, the predefined default "tight" basis sets were chosen and scalar-relativistic effects for all electrons were taken into account within the zero-order regular approximation (ZORA). The ED, ELI-D, and partial ELI-D (pELI)[36,44] were evaluated using the program DGrid[39] on the basis of the obtained wave functions. Scalar fields and the related basins for both Yb_2PdGe_3 and the molecules were visualized with the aid of the ParaView[45,46] application.

3. RESULTS AND DISCUSSION

3.1. Results of SEM/EDXS/XRPD Characterization. Characterization of the $RE_{33.3}Pd_{16.7}Ge_{50.0}$ samples (*RE* = Y, La−Nd, Sm, Gd−Er) confirmed the literature data on the existence of the $RE(Pd_xGe_{1-x})_2$ phases with an average composition close to the 2:1:3 stoichiometry and an AlB_2-like crystal structure, where Pd and Ge share the 2*d* crystallographic site; phases comprising La and Ce turned out to be tetragonal (see Table S1). The Er-containing member of this series is here reported for the first time. As an example, the X-ray powder patterns of $RE(Pd_xGe_{1-x})_2$ phases (*RE* = Ce, Pr, Tb) are shown in Figure S1.

However, the Yb-containing samples, prepared both by metal flux and direct synthesis followed by sintering, showed the presence of the Yb_2PdGe_3 ternary phase (see Table 3) with an ordered superstructure (see Section 3.2 for crystal structure details).

Indium flux turned out to be reactive: in sample #1, Pd_3In_7, Yb_2PdGe_6, recrystallized Ge and the new Yb_2PdGe_3 were detected both by SEM-EDXS (Figure 1a) and X-ray powder diffraction obtained after the flux separation (see Figure S2). The peaks associated to tetragonal In were not revealed in the X-ray powder pattern. Good-quality Yb_2PdGe_3 crystals, showing a plate-like morphology, were detected with SEM/EDXS (Figure 1b) with no traces of In impurities. From this sample, a single crystal was selected for X-ray analysis and structure solution.

Sample #2 was revealed to be Yb_2PdGe_3 single phase (see Figure 1c) with the same crystal structure as in the In-flux synthesized sample.

3.2. Crystal Structure of Yb_2PdGe_3 as the AlB_2 Superstructure. A Yb−Pd−Ge ternary compound of composition ∼33.3 atom % Yb; ∼16.7 atom % Pd; and 50 atom % Ge was reported in the literature[47] as AlB_2-like (*a* = 4.2276(3) Å, *c* = 4.0686(6) Å), as the representatives with other rare-earth components.

The analysis of the collected data highlights that the strongest diffraction peaks are compatible with the AlB_2-type pattern; however, a regular distribution of weak superreflections cannot be neglected; including all of these in the

https://doi.org/10.1021/acs.inorgchem.2c03303
Inorg. Chem. 2023, 62, 1988−1999

indexation, a hexagonal unit cell with $a \sim 8.47$ Å, $c \sim 4.07$ Å is obtained, that is four times bigger than that of the AlB_2 type.

In the reconstructed *hk*0 precession image, the reciprocal space relation between parent and derivative unit cells is evidenced (Figure 2, left); the intensity difference between the main and superreflections is well visible from the 3D plot (Figure 2, right).

The analysis of the systematic absences suggests a primitive lattice centering and numerous possible space groups (*P*6/*mmm*, *P*622, *P*6*mm*, *P*-6, *P*6, etc.). Moreover, the $|E^2 - 1|$ criterion was ~1.4, being noticeably far from the ideal value of 1 (centrosymmetric space group). These observations can be reasonably explained by the elevated number of weak superreflections in the data set. A chemically reasonable structure model was found in the *P*6/*mmm* space group. Further structure refinements were carried out by full-matrix least-squares methods on $|F^2|$ using the SHELXL program package.[28] The site occupancy factors of all species were checked for deficiency, in separate cycles of refinement, obtaining values very close to unity. The final model was additionally checked with PLATON,[48] indicating no missing symmetry elements. At this point, neither deficiency nor the statistical mixture were considered, and the stoichiometric Yb_2PdGe_3 (*hP*12-Ce_2CoSi_3) model was further anisotropically refined, giving acceptable residuals and a flat difference Fourier map. Selected crystallographic data are listed in Table 4.

Table 4. Atomic Coordinates and Equivalent Isotropic Displacement Parameters for the Investigated Yb_2PdGe_3 Single Crystal

atom	site	*x*/*a*	*y*/*b*	*z*/*c*	U_{eq} (Å^2)
Yb1	3*f*	1/2	0	0	0.0107(3)
Yb2	1*a*	0	0	0	0.0090(3)
Pd	2*d*	1/3	2/3	1/2	0.0103(3)
Ge	6*m*	0.16616(2)	0.33232(3)	1/2	0.0108(3)

The structural model was confirmed by X-ray powder diffraction analysis on the Yb_2PdGe_3 sample prepared by direct synthesis followed by sintering. Results of Rietveld refinement on this sample are visualized in Figure 3. Least-squares refinement cycles converged to $R_B = 0.0512$, $R_F = 0.109$, and $\chi^2 = 3.93$, confirming that the diffraction pattern calculated based on the established structural model of Yb_2PdGe_3 is in good agreement with the experimental data. The refined lattice parameters and atomic positions are in good agreement with single-crystal data.

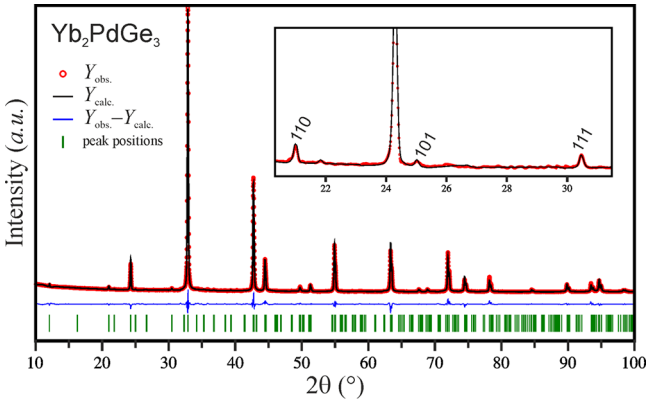

Figure 3. Observed (red circles), calculated (black line), and difference (bottom blue line) X-ray powder diffraction patterns for Yb_2PdGe_3. Indexed superreflections are visible in the inset.

The relationship between AlB_2 (aristotype) and Yb_2PdGe_3 (four-order superstructure) is conveniently represented in terms of a group−subgroup relation already described in ref.[11] Starting from AlB_2, an *isomorphic* transition of index 4 (*i*4) yields to the Yb_2PdGe_3 structure, with doubled *a* and *b* axes (see Figure 4). As a consequence, Yb atoms occupy two

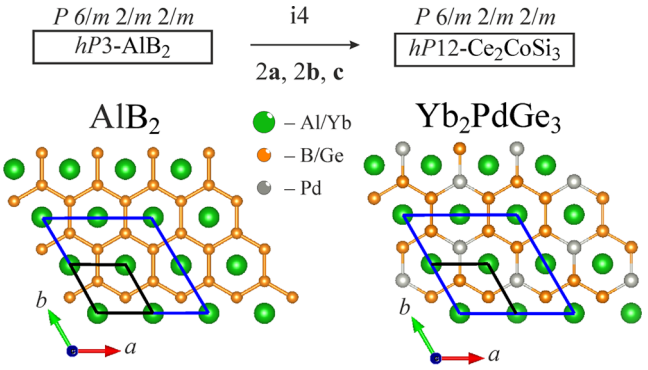

Figure 4. Bärnighausen symmetry reduction step relating the AlB_2 aristotype and its Yb_2PdGe_3 derivative. The graphite-like layers composed of B_6 (AlB_2) and Ge_6/Ge_4Pd_2 (Yb_2PdGe_3) are evidenced. The unit cells shown in black and blue highlight the metric relations between AlB_2 and Yb_2PdGe_3, respectively.

different positions (1*a* and 3*f*), located in the correspondence to the centers of Ge_6 and Ge_4Pd_2 hexagons, respectively, when viewed along the *c* direction. In each Ge_4Pd_2 hexagon, the Pd atoms are placed in *para* positions. Based on Ge−Ge (2.44 Å) and Ge−Pd (2.45 Å) interatomic distances, it is reasonable to interpret their planar layers as covalently bonded. Thus, the study of chemical bonding is of great interest in the framework of the chemistry of inorganic "graphene".[49,50]

The cell volumes of studied phases as a function of the RE^{3+} radius are plotted in Figure 5. A four times smaller cell volume ($V_{cell}/4$) was considered for the Yb_2PdGe_3 superstructure. The general trend is linear, being in line with the lanthanide

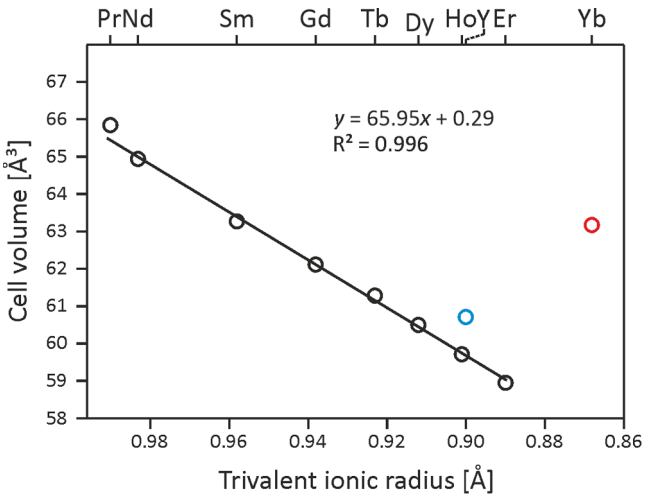

Figure 5. Cell volumes of $RE(Pd_xGe_{1-x})_2$ and Yb_2PdGe_3 (red circle) compounds as a function of the RE^{3+} ionic radius. The blue circle indicates the datum for *RE* = Y.

https://doi.org/10.1021/acs.inorgchem.2c03303
Inorg. Chem. 2023, 62, 1988−1999

contraction (the Y representative was not considered for linear regression). However, the datum for ytterbium is out of trend, suggesting a divalent or intermediated/mixed state for this species and motivating measurements of physical properties. Finally, it is worth noting that the lattice constants found for the $RE(Pd_xGe_{1-x})_2$ phases are in good agreement with those already published.[14]

3.3. Magnetic Properties of Yb_2PdGe_3. The temperature dependence of magnetic susceptibility for Yb_2PdGe_3 is depicted in Figure 6 for different low-DC fields. Both zero-field-cooled (ZFC) and field-cooled (FC) warming cycles were applied revealing a weak Pauli paramagnetism down to ~50 K. The residual susceptibility obtained from a linear approximation corresponds to $\chi_0 = 1.5 \times 10^{-8}$ m^3/mol. The upturn in χ(T) below 50 K is probably due to a minor paramagnetic impurity (i.e., invisible in the powder XRD and EDXS). Below 4.5 K, a strong diamagnetic signal appears due to a transition of Yb_2PdGe_3 into a superconducting state with a critical temperature, T_C = 4 K. The appearance of a magnetic hysteresis (Figure 6 inset) confirms the studied germanide to be a superconductor of type II. The superconducting volume fraction is 94% at 2.5 mT and 7.6% at 5.0 mT (see Figure S3). The hysteresis closes at a second critical field $B_{c2} \approx 80$ mT at 1.8 K. Up to now, in the studied family of compounds, this behavior has only been reported for the Y representative, where a superconducting transition below 3 K was found.[16,19] A more precise estimation of the superconducting parameters will become an object of further study.

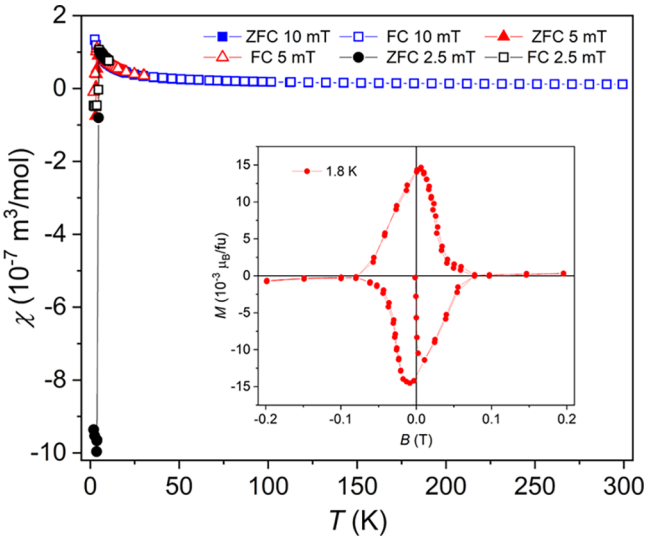

Figure 6. Temperature dependence of the magnetic susceptibility of Yb_2PdGe_3 as ZFC/FC cycles taken at 2.5, 5.0, and 10 mT. Inset corresponds to the field dependence of the magnetization below T_C, at 1.8 K.

3.4. Electronic Structure and Chemical Bonding. Chemical bonding for intermetallic compounds containing *p*-block elements is generally assessed by applying the Zintl–Klemm approach together with a careful crystal-chemical analysis of the polyanionic fragments.

Interatomic Ge–Ge distances (d_{Ge-Ge}) equal to 2.44 Å leave no doubt about the covalent nature of such interactions. As a first approximation, if compared with d_{Ge-Ge} in cubic Ge (2.45 Å),[14] they may be interpreted as single bonds, leading to the following ionic formula with two homopolar bonds per Ge atom: $(Yb^{2+})_2(Pd^{2+})[(2b)Ge^{2-}]_3$. At the same time, the presence of planar, regular Ge_6 hexagons with a $6/mmm$ (D_{6h}) point symmetry hints toward a Hückel-like arene, formally bearing a −6 charge. In this case, the resulting ionic formula is $(Yb^{2+})_4(Pd^-)_2(Ge_6^{6-})$. A deeper analysis of interatomic distances for germanides evidences that, although both hypotheses are in line with the 8 − N rule, an intermediate bonding scenario might be expected. In fact, Ge–Ge single bonds in Zintl-like compounds are generally expected to be longer than 2.45 Å; this effect is often roughly explained, invoking the Coulombic repulsion among negatively charged Ge species.[51] The double-bond length in molecular digermenes was reported to range from 2.20 to 2.50 Å[52] depending on the substituents, being even longer in a few cases. A $[Ge_2]^{4-}$ Zintl dumbbell, with d_{Ge-Ge} = 2.39 Å, was reported by Scherf et al.[51] within the Li_3NaGe_2 phase and described as a solid-state equivalent of O_2. It is worth mentioning another AlB_2 derivative, Ba_2LiGe_3,[53] that possesses Ge_6 rings with d_{Ge-Ge} of 2.51 and 2.52 Å. This elongation with respect to the title compound probably stems from the enhanced charge transfer from the metal species, resulting in Ge_6^{10-} anions, which were described as arene-like π-systems.[53] At this point, a comparison with the simulated aromatic, Ge_6H_6, and Ge_6^{6-} molecular species could give additional insights. In fact, the shortest d_{Ge-Ge} in Yb_2PdGe_3 is intermediate between 2.3 Å (Ge_6H_6) and 2.7 Å (Ge_6^{6-}) (see Table S2 for further details), prompting an intermediate bonding scenario that may be ascribed to additional Ge–Pd/Yb interactions.

This concise survey on interatomic distances shows that a much more complicated bonding scenario than the Zintl one is realized, fostering deeper investigations based on DFT electronic structure calculations. For this purpose, total and species-projected densities of states (DOS and pDOS) were calculated (see Figure 7; the band structure together with the Brillouin zone is shown in Figure S4).

The presence of a pseudogap at the E_F (see the inset in Figure 7) implies that Yb_2PdGe_3 has a metallic behavior. The DOS may be separated into two regions: one below −5.71 eV, which is mainly contributed by the Ge 4*s* states, and the other above, up to E_F. The latter is built up by the Ge 4*p* states that energetically overlap with the Pd and Yb ones, suggesting the

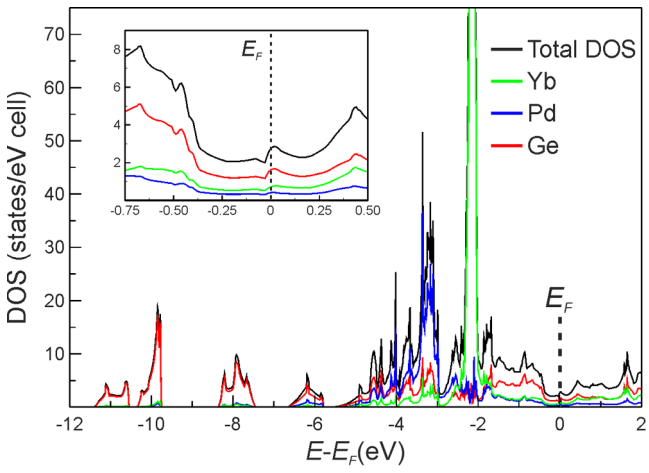

Figure 7. Calculated total and species-projected electronic density of states (DOS/pDOS) for Yb_2PdGe_3. The inset displays details around the Fermi level, which is indicated by a dotted line.

https://doi.org/10.1021/acs.inorgchem.2c03303
Inorg. Chem. 2023, 62, 1988–1999

formation of polar Ge−Pd/Yb bonds. The active participation of the 4*d* states of Pd into chemical bonding is indicated by their width of about 1 eV. Moreover, the *d* state location far from the E_F, between −5 and −4 eV, hints toward a Pd anionic behavior. The narrow peak at about −2.3 eV is due to the localized and fully occupied 4*f* states of both Yb1 and Yb2 species. If the Coulomb parameter *U* is not employed, the 4*f* states are practically located at E_F and display a slight increase of the band width (see Figure S5 for the DOS and pDOS obtained from the LDA calculation). The goodness of the selected *U* parameter is also evident when the (p)DOS curves of Yb_2PdGe_3 are compared with those of Ca_2PdGe_3, calculated using, for consistency, the same computational setup (see Figure S5 to the right). Finally, it is worth noting that although the LSDA + *U* calculations were started with nonzero spin magnetic moments, the self-consistent solution was a nonmagnetic one. These findings support the nonmagnetic nature of the ground state and are consistent with the magnetization data reported in the previous paragraph, revealing a divalent state for Yb species.

To get more insights on chemical bonding, quantum-chemical techniques in position space were selected. The effective QTAIM charges are show in Figure 8. Yb species bear

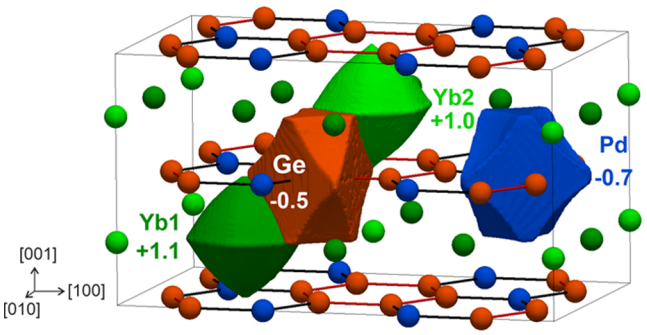

Figure 8. Shapes and effective charges of the QTAIM atomic basins for Yb_2PdGe_3. To enable a clearer view, an ortho-hexagonal cell was employed.

very similar positive charges, i.e., +1.1 for Yb1 and +1.0 for Yb2, and display quasi-spherical shapes, typical for rare-earth and alkaline-earth cations in similar compounds.[54−56]

Their effective charges are quite low if compared with the formal values, suggesting an active participation in chemical bonding. Germanium and palladium are both QTAIM anions and display very similar shapes and charges. In fact, flat surfaces are found for Ge−Ge and Ge−Pd contacts whereas rather convex surfaces point toward the six-coordinating ytterbium atoms. Interestingly, these characteristic features of covalently bonded *p*-block elements are practically identical for both germanium and palladium. Such intriguing anionic behavior of palladium and other transition metals (e.g., Ru, Ir, Pt, Au, Ag) has been increasingly reported in the literature[54,55,57−63] and considered responsible for unprecedented chemical properties.[64,65] Hence, the QTAIM effective charges indicate that the crystal structure of Yb_2PdGe_3 is composed of $^2_\infty$[$PdGe_3$] honeycomb anionic layers spaced by Yb cations.

To shed more light on the interactions among the constituents, a careful analysis of the topology of the Electron Localizability Indicator, in its ELI-D representation,[66,67] was undertaken. Additionally, the crystal space is partitioned into valence and core basins by applying the Bader's mathematical formalism to the ELI-D scalar field. The polarity of valence basins is evaluated through the intersection technique.[68] The contribution, in terms of electronic population, of a QTAIM atom (X) intersecting an ELI-D basin (B_i) is quantified by the bond fraction $p(B_i^X)$.[69,70] The latter are further used to evaluate the covalent, $cc(B_i)$, and lone pair, $lpc(B_i)$, characters[69,70] for each ELI-D valence basin. These tools permit to describe ELI-D basins as lone pairs, nonpolar, and heteropolar bonds, opening the door to a consistent and quantitative treatment of the latter.

In the valence region, the ELI-D attractors are located around the germanium atoms, as shown in Figure 9a,b by means of its planar distribution and isosurfaces, respectively.

The presence of covalent Ge−Ge bonding is confirmed by the ELI-D maxima distribution. A tiny splitting of the attractors is observed for this interaction that does not substantially affect the overall bonding interpretation (more details on this are discussed in Figure S6). Two maxima per germanium atom point toward the neighboring metals and may be interpreted at a first approximation as lone pairs (Figure 9b). No attractors are found along Pd−Ge, so that a graphite-like bonding scenario is unlikely.

The described ELI-D topology composed of two lone pairs and two bonds per germanium is quite characteristic for two-bonded (2*b*) species and has been recently reported for both binary and ternary germanides within Ge zigzag chains (e.g., RE_2MGe_6, CaGe,[58] and LuGe[71]). Nonetheless, interesting differences may be detected when focusing on the average electronic populations. The bonding basins display a larger population than the lone pair ones, i.e., 2.40 vs 1.70 (see Figure 9c). This is in contrast with the expected overpopulation of lone pairs, along with a consequent bonds underpopulation, with respect to the ideal 2.00 electrons (e^-).[58,71,72] A comparative analysis with related intermetallic germanides is helpful; RE_2MGe_6 (M = another metal) compounds are particularly suitable for this purpose due to similar Ge coordination environments (see Figure S7). In Y_2PdGe_6,[58] the population of 1.68 e^-, found in the bonding basin associated to Ge−Ge contacts at 2.45 Å, is significantly lower than the 2.40 e^- for the same basin in the title phase. In the analogous germanides, these populations were found to decrease together with increasing d_{Ge-Ge}, reaching the value of 1.12 e^- for CaGe with a distance of 2.59 Å. Despite the structural similarities, Yb_2PdGe_3 is not following this trend and its enhanced bonding basin population can be considered an indication of a Ge−Ge bond order larger than one.

The bonding basin is intersected by two germanium and four ytterbium QTAIM atoms (see Figure 9d, orange and green portions). The contribution of the Yb species is negligible (0.12 e^- in total) so that it is an effectively two-atomic (2*a*) interaction. In accordance with its nonpolar nature, the $cc(B_i)$ is equal to 1. The valence basins indicated up to this point as "lone pairs" are intersected by 1Ge, 1Pd, 2Yb1, and 1Yb2. The main contribution comes from Ge, followed by Pd, leading to bond fraction values of 0.73 and 0.20, respectively, hinting toward a polar covalent bond rather than a lone pair. Whereas the Yb2 contribution should be neglected (0.012 e^-), a different scenario is realized by the two Yb1 species. In fact, they yield a total bond fraction of 0.06 (0.03 per Yb2 atom), allowing to describe this basin as four-atomic (4*a*). Analogous bond fractions were recently reported for CaGe[58] (0.08 per 4Ca atoms), where each Ge "lone pair"

https://doi.org/10.1021/acs.inorgchem.2c03303
Inorg. Chem. 2023, 62, 1988−1999

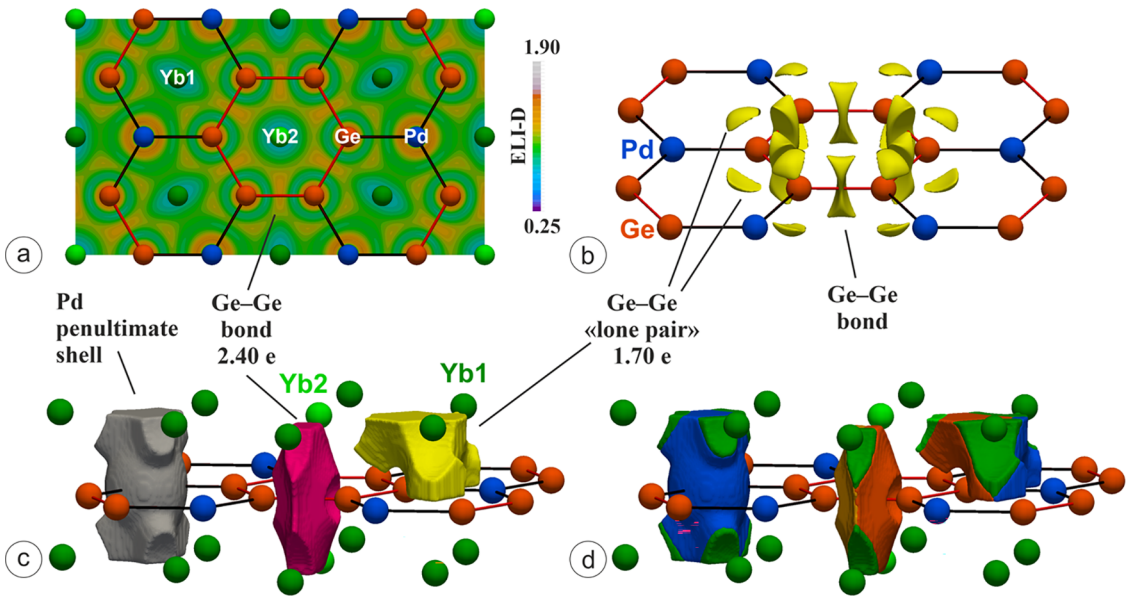

Figure 9. (a) ELI-D distribution within the (001) plane and (b) isosurfaces enclosing 1.176-localization domains; (c) shape of the ELI-D basins; (d) intersection of the ELI-D basins by QTAIM atoms; the coloring scheme for the intersected regions follows that chosen for the atoms and QTAIM basins. Average electronic populations of selected ELI-D basins are also indicated.

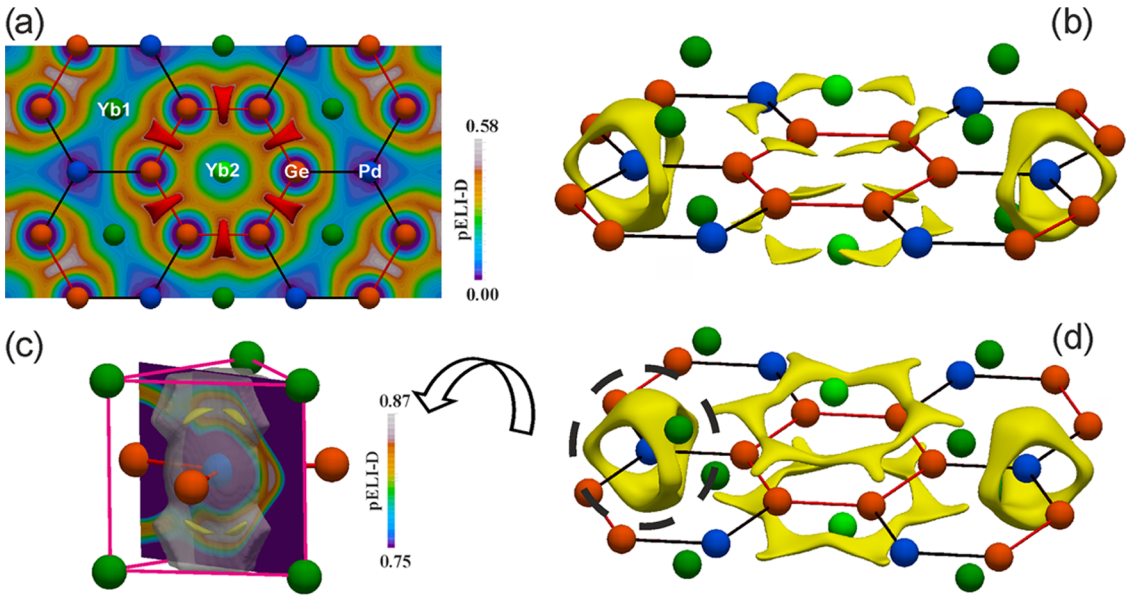

Figure 10. Partial ELI-D (pELI) contributions for A (−12.0 to −5.71 eV) and B (−5.71 to E_F) DOS regions: (a) slice with pELI distribution derived from region A in the honeycomb layer together with red isosurfaces enclosing 0.46-localization domains; (b–d) yellow pELI isosurfaces derived from region B enclosing 0.833- (b), 0.867- (c), and 0.823-localization domains (d). The penultimate shell ELI-D basin of Pd is shown as well (c).

was definitely interpreted as a 5*a*-Ge_1Ca_4 basin after the application of the Penultimate Shell Correction method (PSC0), leading to a bond fraction of 0.15. Such approach was introduced to account for the rare-earth underestimated contributions due to a considerable charge storage in the penultimate shell. The same effect, although less severe, was reported for Ca, which displayed a core overpopulation of about 0.3 e^-; for the actual calculations, a storage of 0.4 e^- was obtained for Yb. The PSC0 approach is still not applicable to compounds containing transition metals with an ambiguous oxidation state, such as Pd. The $cc(B_i)$ and $lpc(B_i)$ for such 4*a*-$Ge_1Pd_1Yb1_2$ heteropolar bond are almost equal, being 0.53 and 0.47, respectively, supporting its covalent nature.

The shape of the Pd penultimate shell basin deserves further comments. It has six bulges that extend in the valence region (see Figure 9c) toward the six adjacent Yb1 species. In fact, each bulge is intersected by the corresponding Yb1 QTAIM atom (see dark green regions in Figure 9d). This kind of feature was observed for ternary intermetallics both with germanium, such as La_2MGe_6 (M = Pd, Ag)[58] and without germanium, such as $LaAuMg_2$,[55] and described as 2*a* polar covalent metal–metal bonds, as also confirmed by the ELI-D relative Laplacian. Considering this, each Pd is covalently bonded with the six neighboring Yb1 species, located on the vertices of the trigonal coordination prism. The realization of *RE*–Pd covalent interactions was also reported for some

https://doi.org/10.1021/acs.inorgchem.2c03303
Inorg. Chem. 2023, 62, 1988–1999

related ternary germanides on the basis of different quantum-chemical approaches.[54,73]

3.5. Additional Details on Chemical Bonding: From Molecules to Solid State. Further interesting details may be obtained analyzing the partial ELI-D (pELI, see Figure 10)[44,67] that is calculated from the EDs obtained from separated states located in two DOS energy ranges (see Figure S8), indicated in the following with letters A (-12.0 eV $< E < -5.71$ eV) and B (-5.71 eV $< E <$ 0.00 eV).

Region A was selected since it is mainly dominated by the Ge 4*s* states and follows the same energy sequence found in the orbital schemes of Ge_6H_6 and Ge_6^{6-} (red orbitals in Figure 11).

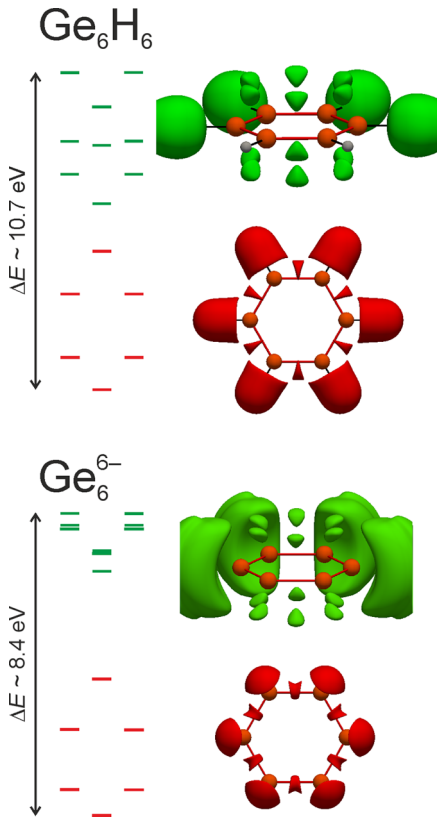

Figure 11. Molecular orbital energy diagrams of Ge_6H_6 (top) and Ge_6^{6-} (bottom), together with pELI contributions. In the two figures representing pELI contributions derived from the highest energy orbitals (green), two domains in the exocyclic regions have been deleted to enable a better view for the reader.

In fact, states in A are separated into four bands populated by 2, 4, 4, and 2 e^- per Ge_6 ring of Yb_2PdGe_3. Thus, a comparative bonding analysis among the title crystalline solid and the molecules is enabled by the pELI function, which allows to recover orbital contributions in position space. Such comparison is even more interesting, keeping in mind that the two molecules both show one a_{2u} and two e_{1g} molecular orbitals with a shape characteristic for aromatic six-membered rings (see Figure S9). At this point, it is worth mentioning that based on computed magnetic criteria, it has been proven that Ge_6H_6, as its Si_6H_6 analogue, is less aromatic than benzene so that a nonplanar $\bar{3}m$ (D_{3d}) cyclic molecule is expected to be energetically favored.[74] When the molecular structure optimization was performed starting from a planar 6/*mmm* molecule, it converges to a local energy minimum retaining the desired symmetry. On the contrary, if one Ge atom is located out of the plane, the final structure is the favored one being more stable by -0.563 eV (PW), -0.768 eV (PBE), and -0.784 eV (B3LYP) than 6/*mmm*, in accordance with the literature.[74] Aiming at performing a consistent analysis, all-electron wave functions obtained from LDA/PW calculations were used for the comparative study. However, no relevant differences were detected among ELI and pELI calculated on the basis of the wave functions obtained employing the PBE or B3LYP functional.

Coming back to Yb_2PdGe_3, the states in the A energy interval of the DOS display pELI contribution only around the Ge_6 ring on its very same plane (see pELI planar distribution in Figure 10a), with maxima located between the Ge−Ge contacts (red isosurfaces in Figure 10a). The pELI distribution resulting from the six energetically lower valence orbitals of Ge_6H_6 and Ge_6^{6-} is analogue (red isosurfaces in Figure 11).

It is not straightforward to extend this analysis to the remaining energy range. In fact, the B region of the DOS is not separated into bands so that it is not trivial to compare it with the discrete orbitals of the reference molecules. Hence, clear differences are expected to occur between the pELI contributions coming from the B interval of the DOS and the remaining nine valence MOs of the molecules, indicated by green bars in Figure 11. They are formed by a linear combination of Ge 4*p* and H 1*s* for Ge_6H_6 and just by the Ge 4*p* for Ge_6^{6-}. The resulting pELI (see green isosurfaces in Figure 11) distributions are practically identical and show two kinds of attractors: the first are symmetrically located above and below the mid-point of the Ge−Ge bond, representing the π-interactions; the second are in the exocyclic region signifying Ge−H bonds in the case of Ge_6H_6 and Ge lone pairs for Ge_6^{6-}. As expected, a somewhat different picture is obtained for Yb_2PdGe_3. The pELI attractors are still symmetrically positioned above and below the Ge_6 planes but find their location in correspondence of the Ge atoms and not among them (see yellow isosurfaces in Figure 10b). Thus, they seem to indicate the polar interactions between Ge and the surrounding metals. Nevertheless, the visualization of pELI isosurfaces at lower values reveals two reducible localization domains spreading over the whole Ge_6 fragments above and below their plane, pointing out rather high pELI contributions also in these regions. Such feature supports the idea of some π-interactions among the Ge atoms, even if reduced with respect to the selected molecular references. Consequently, the bonding scenario appears to be intermediate between that of a typical 2c−2e Ge−Ge bond and an aromatic picture, well in line with the conclusions drawn from the interatomic distances and the ELI-D basin population analysis.

Finally, the pELI distribution from the DOS region B gives some insights into the Pd−Yb bonds as well. Six pELI maxima around each palladium point toward the neighboring Yb, as displayed by the 0.867-irreducible localization domains shown in Figure 10c. When such attractors are visualized superimposed with the Pd penultimate shell basins (gray transparent basin in Figure 10c), they are located in the spatial region corresponding to the bulges. This finding is not just supporting the formation of Pd−Yb bonds but constitutes one more evidence of the correct afore-given interpretation of the bulges of ELI-D penultimate shell basins.

https://doi.org/10.1021/acs.inorgchem.2c03303
Inorg. Chem. 2023, 62, 1988−1999

4. CONCLUSIONS

Ternary rare-earth germanides of nominal composition $RE_{33.3}Pd_{16.7}Ge_{50.0}$ were reinvestigated along the *RE* series (*RE* = Y, La−Nd, Sm, Gd−Er, Yb) aiming at checking for the existence of ordered structures. The existence of the $RE(Pd_xGe_{1-x})_2$ disordered phases, crystallizing with the *hP*3-AlB_2 structure, has been confirmed with all *RE*, but Yb. X-ray diffraction analyses both on powders and single crystals, indicate that the Yb_2PdGe_3 compound is a four-order superstructure of AlB_2, crystallizing with the *hP*12-Ce_2CoSi_3 type of structure. Based on refined structural data and the calculated QTAIM effective charges, the crystal structure may be described as composed of two-dimensional $^2_\infty[PdGe_3]$ honeycomb anionic layers spaced by Yb cations. Both DFT/LSDA + *U* calculations and measured magnetic susceptibility as a function of temperature hint toward a divalent state of Yb. Moreover, Yb_2PdGe_3 displays a type-II superconducting behavior below the critical temperature of 4 K, a feature shared only with the disordered $Y(Pd_xGe_{1-x})_2$ phase. Position-space chemical bonding analysis indicates, in addition to homopolar Ge−Ge bonds, polar four-atomic $Ge_1Pd_1Yb_2$ and two-atomic Pd−Yb bonds. Further insights, with main regards to the nature of Ge−Ge interactions within regular Ge_6 hexagons, were obtained by analyzing the partial ELI-D field that enabled a comparison between the crystalline Yb_2PdGe_3 and the hypothetic Ge_6H_6 and Ge_6^{6-} molecules. Finally, a bond order larger than one is proposed for Ge−Ge bonds, suggesting a bonding scenario intermediate between that of a typical 2c−2e Ge−Ge bond and an aromatic behavior. Such results extend the chemistry of inorganic germanium and enrich with one more representative the bonding outcomes for ternary *RE*−Pd−Ge, which shows similar features like multiatomic interactions involving all species and *RE*−Pd bonds, here presented for the first time with *RE* = Yb. The search for appropriate doping, able to increase the measured critical temperature, and for new RE_2TGe_3 representative, displaying intriguing physical and chemical properties, is ongoing.

■ ASSOCIATED CONTENT

Supporting Information

The Supporting Information is available free of charge at https://pubs.acs.org/doi/10.1021/acs.inorgchem.2c03303.

Results of EDXS and XRPD analysis for *RE*−Pd−Ge samples, X-ray powder patterns for some representative samples, optimized structural data for the simulated Ge_6H_6 and Ge_6^{6-} molecules, superconducting volume fraction, band structure and Brillouin zone for Yb_2PdGe_3, DOS and pDOS for Yb_2PdGe_3 and Ca_2PdGe_3 based on both DFT and DFT + *U* calculations, ELI-D attractors splitting along the Ge−Ge contacts, structural similarities among Yb_2PdGe_3 and Yb_2PdGe_6, DOS energy windows selected to calculate the pELI-D of Yb_2PdGe_3, and π molecular orbitals of the simulated Ge_6H_6 and Ge_6^{6-} molecules (PDF)

Accession Codes

CCDC 2230957 contains the supplementary crystallographic data for this paper. These data can be obtained free of charge via www.ccdc.cam.ac.uk/data_request/cif, or by emailing data_request@ccdc.cam.ac.uk, or by contacting The Cambridge Crystallographic Data Centre, 12 Union Road, Cambridge CB2 1EZ, UK; fax: +44 1223 336033.

■ AUTHOR INFORMATION

Corresponding Author

Riccardo Freccero − *Dipartimento di Chimica e Chimica Industriale, Università degli Studi di Genova, I-16146 Genova, Italy;* orcid.org/0000-0003-4273-1218; Email: riccardo.freccero@.unige.it

Authors

Laura C. J. Pereira − *Centro de Ciências e Tecnologias Nucleares, Department of Engenharia e Ciências Nucleares, Instituto Superior Técnico, Universidade Lisboa, 2695-066 Bobadela, Portugal;* orcid.org/0000-0002-8818-0039

Pavlo Solokha − *Dipartimento di Chimica e Chimica Industriale, Università degli Studi di Genova, I-16146 Genova, Italy;* orcid.org/0000-0002-5252-635X

Serena De Negri − *Dipartimento di Chimica e Chimica Industriale, Università degli Studi di Genova, I-16146 Genova, Italy;* orcid.org/0000-0002-5345-8694

Complete contact information is available at: https://pubs.acs.org/10.1021/acs.inorgchem.2c03303

Notes

The authors declare no competing financial interest.

■ ACKNOWLEDGMENTS

The authors thank D. M. Proserpio (Università degli Studi di Milano, Italy) for providing access to the single-crystal diffractometer. L.C.J.P. thanks the Portuguese National Funding Agency for Science, and Technology, FCT, under Projects UID/Multi/04349/2020 and LISBOA-01-0145-FEDER-022096.

■ REFERENCES

(1) Lin, Q.; Miller, G. J. Electron-Poor Polar Intermetallics: Complex Structures, Novel Clusters, and Intriguing Bonding with Pronounced Electron Delocalization. *Acc. Chem. Res.* **2018**, *51*, 49−58.

(2) Gumeniuk, R.; Schöneich, M.; Kvashnina, K. O.; Akselrud, L.; Tsirlin, A. A.; Nicklas, M.; Schnelle, W.; Janson, O.; Zheng, Q.; Curfs, C.; Burkhardt, U.; Schwarz, U.; Leithe-Jasper, A. Intermetallic Germanides with Non-Centrosymmetric Structures Derived from the $Yb_3Rh_4Sn_{13}$ Type. *Dalton Trans.* **2015**, *44*, 5638−5651.

(3) Giovannini, M.; Curlík, I.; Freccero, R.; Solokha, P.; Reiffers, M.; Sereni, J. Crystal Structure and Magnetism of Noncentrosymmetric Eu_2Pd_2Sn. *Inorg. Chem* **2021**, *60*, 8085−8092.

(4) Chen, J.; Gamza, M. B.; Banda, J.; Murphy, K.; Tarrant, J.; Brando, M.; Grosche, F. M. Unconventional Bulk Superconductivity in YFe_2Ge_2 Single Crystals. *Phys. Rev. Lett.* **2020**, *125*, No. 237002.

(5) Roychowdhury, S.; Ochs, A. M.; Guin, S. N.; Samanta, K.; Noky, J.; Shekhar, C.; Vergniory, M. G.; Goldberger, J. E.; Felser, C. Large Room Temperature Anomalous Transverse Thermoelectric Effect in Kagome Antiferromagnet YMn_6Sn_6. *Adv. Mater.* **2022**, *34*, No. 2201350.

(6) Lin, Q.; Aguirre, K.; Saunders, S. M.; Hackett, T. A.; Liu, Y.; Taufour, V.; Paudyal, D.; Budko, S.; Canfield, P. C.; Miller, G. J. Polar Intermetallics $Pr_5Co_2Ge_3$ and $Pr_7Co_2Ge_4$ with Planar Hydrocarbon-Like Metal Clusters. *Chem. − Eur. J.* **2017**, *23*, 10516−10521.

(7) Freccero, R. *Study of New Ternary Rare-Earth Intermetallic Germanides with Polar Covalent Bonding*; Springer International Publishing: Cham, 2020.

(8) Oliynyk, A. O.; Stoyko, S. S.; Mar, A. Ternary Rare-Earth Ruthenium and Iridium Germanides $RE_3M_2Ge_3$ (RE = Y, Gd−Tm, Lu; M = Ru, Ir). *J. Solid State Chem.* **2013**, *202*, 241−249.
(9) Solokha, P.; De Negri, S.; Proserpio, D. M.; Blatov, V. A.; Saccone, A. Vacancy Ordering as a Driving Factor for Structural Change in Ternary Germanides: The $R_2Zn_{1-x}Ge_6$ Series of Polar Intermetallics (R = Rare-Earth Metal). *Inorg. Chem.* **2015**, *54*, 2411−2424.
(10) Penc, B.; Baran, S.; Hoser, A.; Szytuła, A. Magnetic Properties and Magnetic Structures of R_2TGe_6 (T = Ni, Cu; R = Tb, Ho and Er). *J. Alloys Compd.* **2019**, *803*, 307−313.
(11) Hoffmann, R. D.; Pöttgen, R. AlB_2-Related Intermetallic Compounds - A Comprehensive View Based on Group-Subgroup Relations. *Z. Kristallogr. − Cryst. Mater.* **2001**, *216*, 127−145.
(12) Nagamatsu, J.; Nakagawa, N.; Muranaka, T.; Zenitani, Y.; Akimitsu, J. Superconductivity at 39 K in Magnesium Diboride. *Nature* **2001**, *410*, 63−64.
(13) Pan, Z.-Y.; Cao, C.-D.; Bai, X.-J.; Song, R.-B.; Zheng, J.-B.; Duan, L.-B. Structures and Physical Properties of R_2TX_3 Compounds. *Chin. Phys. B* **2013**, *22*, No. 056102.
(14) Villars, P.; Cenzual, K.*Pearson's Crystal Data: Crystal Structure Database for Inorganic Compounds*; ASM International: Materials Park, OH, 2022.
(15) Rossi, D.; Ferro, R. Ternary Rare Earth (R) Alloys Occurring in Some ~$RPd_{2-x}Ge_x$ Sections. *Intermetallics* **2002**, *10*, 399−402.
(16) Majumdar, S.; Sampathkumaran, E. V. Observation of Enhanced Magnetic Transition Temperature in Nd_2PdGe_3 and Superconductivity in Y_2PdGe_3. *Phys. Rev. B* **2001**, *63*, No. 172407.
(17) Szytuła, A.; Hofmann, M.; Penc, B.; Ślaski, M.; Majumdar, S.; Sampathkumaran, E. V.; Zygmunt, A. Magnetic Behaviour of R_2PdSi_3 Compounds with R=Ce, Nd, Tb−Er. *J. Magn. Magn. Mater.* **1999**, *202*, 365−375.
(18) Jones, C. D. W.; Gordon, R. A.; DiSalvo, F. J.; Pöttgen, R.; Kremer, R. K. Magnetic Behaviour of Two AlB_2-Related Germanides: $CePd_{0.63}Ge_{1.37}$ and $CeAu_{0.75}Ge_{1.25}$. *J. Alloys Compd.* **1997**, *260*, 50−55.
(19) Sampathkumaran, E. V.; Majumdar, S.; Schneider, W.; Molodtsov, S. L.; Laubschat, C. Superconductivity in Y_2PdGe_3. *Phys. B: Condens. Matter* **2002**, *312−313*, 152−154.
(20) Nesper, R.; Curda, J.; Von Schnering, H. G. Li_8MgSi_6, a Novel Zintl Compound Containing Quasi-Aromatic Si_5 Rings. *J. Solid State Chem.* **1986**, *62*, 199−206.
(21) Nesper, R.; Antonio, C.; Wengert, S. Nonaromatic Planar Si_{12} Ring System of Approximate D_{6h} Symmetry in $Ca_7Mg_{7.5\pm\delta}Si_{14}$. *Chem. − Eur. J.* **1998**, *4*, 2251.
(22) Lupu, C.; Downie, C.; Guloy, A. M.; Albright, T. A.; Mao, J. G. $Li_{17}Ag_3Sn_6$: A Polar Intermetallic π-System with Carbonate-like $[AgSn_3]^{11-}$ Anions and Trefoil Aromatic $[Ag_2Sn_3]^{6-}$ Layers. *J. Am. Chem. Soc.* **2004**, *126*, 4386−4397.
(23) *APEX4 V2021.10-0*; Bruker AXS Inc.: Madison, WI, 2021.
(24) *SAINT v8.30A*; Bruker AXS Inc.: Madison, WI, 2012.
(25) *XPREP V2014/2*; Bruker AXS Inc.: Madison, WI, 2014.
(26) *SADABS V2016/2*; Bruker AXS Inc.: Madison, WI, 2016.
(27) Petrícek, V.; Dušek, M.; Palatinus, L. Crystallographic Computing System JANA2006: General Features. *Z. Kristallogr.* **2014**, *229*, 345−352.
(28) Sheldrick, G. M.*SHELXL-2019/1*; Bruker AXS Inc.: Madison, WI, 2019.
(29) Rodriguez-Carvajal, J. FullProf. *IUCr Newsl.* **2001**, *26*, 12−19.
(30) Eschrig, H.; Koepernik, K.; Chaplygin, I. Density Functional Application to Strongly Correlated Electron Systems. *J. Solid State Chem.* **2003**, *176*, 482−495.
(31) Koepernik, K.; Eschrig, H. Full-Potential Nonorthogonal Local-Orbital Minimum-Basis Band-Structure Scheme. *Phys. Rev. B* **1999**, *59*, 1743−1757.
(32) Perdew, J. P.; Wang, Y. Accurate and Simple Analytic Representation of the Electron-Gas Correlation Energy. *Phys. Rev. B* **1992**, *45*, 13244−13249.
(33) Juckel, M.; Koželj, P.; Prots, Y.; Ormeci, A.; Burkhardt, U.; Leithe-Jasper, A.; Svanidze, E. Intermediate Valence Behavior of $Yb_2Cu_9Al_8$. *Z. Anorg. Allg. Chem.* **2020**, *646*, 1238−1243.
(34) Grin, Y.; Pöttgen, R.; Ormeci, A.; Kremer, R. K.; Wagner, F. E. Intermediate-Valence Intermetallic Phase $YbIn_{1-x}Au_{1+x}$(x = 0-0.3). *Cryst. Technol.* **2017**, *52*, No. 1700101.
(35) Kohout, M. A Measure of Electron Localizability. *Int. J. Quantum Chem.* **2004**, *97*, 651−658.
(36) Wagner, F. R.; Bezugly, V.; Kohout, M.; Grin, Y. Charge Decomposition Analysis of the Electron Localizability Indicator: A Bridge between the Orbital and Direct Space Representation of the Chemical Bond. *Chem. − Eur. J.* **2007**, *13*, 5724−5741.
(37) Wagner, F. R.; Kohout, M.; Grin, Y. Direct Space Decomposition of ELI-D: Interplay of Charge Density and Pair-Volume Function for Different Bonding Situations. *J. Phys. Chem. A* **2008**, *112*, 9814−9828.
(38) Kohout, M.DGrid-4.6, 2014.
(39) Kohout, M.DGrid-5.0, 2018.
(40) Ormeci, A.; Rosner, H.; Wagner, F. R.; Kohout, M.; Grin, Y. Electron Localization Function in Full-Potential Representation for Crystalline Materials. *J. Phys. Chem. A* **2006**, *110*, 1100−1105.
(41) Bader, R. F. W.*Atoms in Molecules − A Quantum Theory*; Oxford University Press: New York, 1990.
(42) Perdew, J. P.; Burke, K.; Ernzerhof, M. Generalized Gradient Approximation Made Simple. *Phys. Rev. Lett.* **1996**, *77*, 3865−3868.
(43) Vosko, S. H.; Wilk, L.; Nusair, M. Accurate Spin-Dependent Electron Liquid Correlation Energies for Local Spin Density Calculations: A Critical Analysis. *Can. J. Phys.* **1980**, *58*, 1200−1211.
(44) Börrnert, C.; Grin, Y.; Wagner, F. R. Position-Space Bonding Indicators for Hexaborides of Alkali, Alkaline-Earth, and Rare-Earth Metals in Comparison to the Molecular Crystal $K_2[B_6H_6]$. *Z. Anorg. Allg. Chem.* **2013**, *639*, 2013−2024.
(45) Baranov, A.Visualization Plugin for ParaView, 2015.
(46) Ayachit, U.*The ParaView Guide: A Parallel Visualization Application*Kitware; 2015.
(47) Seropegin, Y. D.; Borisenko, O. L.; Bodak, O. I.; Nikiforov, V. N.; Kovachikova, M. V.; Kochetkov, Y. V. Investigation of Phase Relationships and Physical Properties of Yb□Pd□Ge Compounds. *J. Alloys Compd.* **1995**, *216*, 259−263.
(48) Spek, A. L. Structure Validation in Chemical Crystallography. *Acta Crystallogr., Sect. D* **2009**, *65*, 148−155.
(49) Miller, G. J.; Schmidt, M. W.; Wang, F.; You, T. S. Quantitative Advances in the Zintl−Klemm Formalism. *Struct. Bond.* **2011**, *139*, 1−55.
(50) You, T. S.; Miller, G. J. Theoretical Interpretation of the Structural Variations along the $Eu(Zn_{1-x}Ge_x)_2$ ($0 < x < 1$) Series. *Inorg. Chem.* **2009**, *48*, 6391−6401.
(51) Scherf, L. M.; Karttunen, A. J.; Pecher, O.; Magusin, P. C. M. M.; Grey, C. P.; Fässler, T. F. $[Ge_2]^{4-}$ Dumbbells with Very Short Ge−Ge Distances in the Zintl Phase Li_3NaGe_2: A Solid-State Equivalent to Molecular O_2. *Angew. Chem., Int. Ed.* **2016**, *55*, 1075−1079.
(52) Lee, V. Y. Digermenes >Ge=Ge<, Distannenes >Sn=Sn<and Diplumbenes >Pb=Pb<. *Chem* **2012**, *2*, 35−46.
(53) von Schnering, H. G.; von Bolle, U.; Curda, J.; Peters, K.; Carrillo-Cabrera, W.; Somer, M.; Schultheiss, M.; Wedig, U. Hückel-Arene Mit Zehn π-Elektronen: Die Cyclischen Zintl-Anionen Si_6^{10-} Und Ge_6^{10-}, Isoster Mit P_6^{4-} Und As_6^{4-}. *Angew. Chem.* **1996**, *108*, 1062−1064.
(54) Freccero, R.; De Negri, S.; Rogl, G.; Binder, G.; Michor, H.; Rogl, P. F.; Saccone, A.; Solokha, P. $La_2Pd_3Ge_5$ and $Nd_2Pd_3Ge_5$ Compounds: Chemical Bonding and Physical Properties. *Inorg. Chem.* **2021**, *60*, 3345−3354.
(55) Freccero, R.; De Negri, S.; Saccone, A.; Solokha, P. Solid State Interactions in the La-Au-Mg System: Phase Equilibria, Novel Compounds and Chemical Bonding. *Dalton Trans.* **2020**, *49*, 12056−12067.

https://doi.org/10.1021/acs.inorgchem.2c03303
Inorg. Chem. 2023, 62, 1988−1999

(56) Schwarz, U.; Castillo, R.; Hübner, J. M.; Wosylus, A.; Prots, Y.; Bobnar, M.; Grin, Y. The Untypical High-Pressure Zintl Phase $SrGe_6$. *Z. Naturforsch. B* **2020**, *75*, 209−216.
(57) Grin, Y.; Armbrüster, M.; Baranov, A. I.; Finzel, K.; Kohout, M.; Ormeci, A.; Rosner, H.; Wagner, F. R. Atomic Interactions in the Intermetallic Catalyst GaPd. *Mol. Phys.* **2016**, *114*, 1250−1259.
(58) Freccero, R.; Solokha, P.; De Negri, S.; Saccone, A.; Grin, Y.; Wagner, F. R. Polar-Covalent Bonding Beyond the Zintl Picture in Intermetallic Rare-Earth Germanides. *Chem. − Eur. J.* **2019**, *25*, 6600−6612.
(59) Freccero, R.; Solokha, P.; De Negri, S. Unpredicted but It Exists: Trigonal Sc_2Ru with a Significant Metal-Metal Charge Transfer. *Inorg. Chem.* **2021**, *60*, 10084−10088.
(60) Agnarelli, L.; Prots, Y.; Schmidt, M.; Krnel, M.; Svanidze, E.; Burkhardt, U.; Leithe-Jasper, A.; Grin, Y. Be_3Ru: Polar Multiatomic Bonding in the Closest Packing of Atoms. *ChemistryOpen* **2022**, *11*, No. 2200118.
(61) Amon, A.; Svanidze, E.; Ormeci, A.; König, M.; Kasinathan, D.; Takegami, D.; Prots, Y.; Liao, Y.; Tsuei, K.; Tjeng, L. H.; Leithe-Jasper, A.; Grin, Yu. Interplay of Atomic Interactions in the Intermetallic Semiconductor Be_5Pt. *Angew. Chem., Int. Ed.* **2019**, *58*, 15928−15933.
(62) Sichevych, O.; Prots, Y.; Schnelle, W.; Wagner, F. R.; Grin, Y. Polycation-Polyanion Architecture of the Intermetallic Compound $Mg_{3-x}Ga_{1+x}Ir$. *Molecules* **2022**, *27*, 659.
(63) Solokha, P.; Eremin, R. A.; Leisegang, T.; Proserpio, D. M.; Akhmetshina, T.; Gurskaya, A.; Saccone, A.; De Negri, S. New Quasicrystal Approximant in the Sc−Pd System: From Topological Data Mining to the Bench. *Chem. Mater.* **2020**, *32*, 1064−1079.
(64) Jiménez, A. M. B.; Ormeci, A.; Burkhardt, U.; Altendorf, S. G.; Kaiser, F.; Veremchuk, I.; Auffermann, G.; Grin, Y.; Antonyshyn, I. Intermetallic Compounds M_2Pt (M = Al, Ga, In, Sn) in the Oxygen Evolution Reaction. *Sustainable Energy Fuels* **2021**, *5*, 5762−5772.
(65) Antonyshyn, I.; Sichevych, O.; Rasim, K.; Ormeci, A.; Burkhardt, U.; Titlbach, S.; Schunk, S. A.; Armbrüster, M.; Grin, Y. Anisotropic Reactivity of CaAg under Ethylene Epoxidation Conditions. *Inorg. Chem.* **2018**, *57*, 10821−10831.
(66) Kohout, M. A Measure of Electron Localizability. *Int. J. Quantum Chem.* **2004**, *97*, 651−658.
(67) Wagner, F. R.; Bezugly, V.; Kohout, M.; Grin, Y. Charge Decomposition Analysis of the Electron Localizability Indicator: A Bridge between the Orbital and Direct Space Representation of the Chemical Bond. *Chem. − Eur. J.* **2007**, *13*, 5724−5741.
(68) Raub, S.; Jansen, G. A Quantitative Measure of Bond Polarity from the Electron Localization Function and the Theory of Atoms in Molecules. *Theor. Chem. Acc.* **2001**, *106*, 223−232.
(69) Bende, D.; Wagner, F. R.; Grin, Y. 8 - N Rule and Chemical Bonding in Main-Group Mgagas-Type Compounds. *Inorg. Chem.* **2015**, *54*, 3970−3978.
(70) Wagner, F. R.; Bende, D.; Grin, Y. Heteropolar Bonding and a Position-Space Representation of the 8 − N Rule. *Dalton Trans.* **2016**, *45*, 3236−3243.
(71) Freccero, R.; Hübner, J.-M.; Prots, Y.; Schnelle, W.; Schmidt, M.; Wagner, F. R.; Schwarz, U.; Grin, Y. "Excess" Electrons in LuGe. *Angew. Chem., Int. Ed.* **2021**, *60*, 6457−6461.
(72) Zheng, Q.; Wagner, F. R.; Ormeci, A.; Prots, Y.; Burkhardt, U.; Schmidt, M.; Schnelle, W.; Grin, Y.; Leithe-Jasper, A. Interpenetration of a 3D Icosahedral $M@Ni_{12}$ (M=Al, Ga) Framework with Porphyrin-Reminiscent Boron Layers in MNi_9B_8. *Chem. − Eur. J.* **2015**, *21*, 16532−16540.
(73) Freccero, R.; Solokha, P.; Proserpio, D.; Saccone, A.; De Negri, S. Lu5Pd4Ge8 and Lu3Pd4Ge4: Two More Germanides among Polar Intermetallics. *Crystals* **2018**, *8*, 205.
(74) von Ragué Schleyer, P.; Schleyer, R.; Jiao, H.; Van, N. J. R.; Hommes, E.; Malkin, V. G.; Malkina, O. L. An Evaluation of the Aromaticity of Inorganic Rings: Refined Evidence from Magnetic Properties. *J. Am. Chem. Soc.* **1997**, *119*, 12669−12670.

https://doi.org/10.1021/acs.inorgchem.2c03303
Inorg. Chem. 2023, 62, 1988−1999